Full Length Article

Direct growth of graphene-MoS$_2$ heterostructure: Tailored interface for advanced devices

Roberto Muñoz [*], Elena López-Elvira, Carmen Munuera, Riccardo Frisenda, Carlos Sánchez-Sánchez, José Ángel Martín-Gago, Mar García-Hernández

Materials Science Factory, Instituto de Ciencia de Materiales de Madrid, (ICMM-CSIC), Sor Juana Inés de la Cruz 3, E-28049 Madrid, Spain

ABSTRACT

Ultrathin film heterostructures represent the main foundations of numerous modern devices. Recently, 2D materials combined into van der Waals multilayers have emerged as an appealing option to conform heterostructures with outstanding properties while circumventing the interfacial lattice-matching constraints encountered in heteroepitaxial synthesis. Among them, the MoS$_2$-Graphene heterostructures exhibit suitable contact properties that promote efficient charge injection and transfer. We here report on the direct synthesis of graphene films on MoS$_2$ by Plasma Assisted CVD. We assess the influence of using Sulphur vapor during the synthesis to heal the S vacancies, both of natural origin and induced during the growth. We find that the graphene grain size increases when using S and relate this effect with the defect density of MoS$_2$ and the interfacial conductance. The methodologies shown are intrinsically scalable and represent a step forward in the direct growth of van der Waals heterostructures for advanced devices.

1. Introduction

Conventional heteroepitaxial growth is limited to materials with coincident lattice constants in order to reduce interfacial defects or dislocations that impair the performance. Two-dimensional (2D) materials offer a new platform that allows formation of vertical heterostructures held together by van der Waals forces [1]. In proof of concept devices, 2D heterostructures are fabricated by directly stacking mechanically exfoliated flakes of selected materials [2,3]. Microscopy studies demonstrate that interfaces can be atomically flat and free of contamination in localized areas by the so-called "self-cleaning" mechanism [1,4]. A plethora of electronic and photonic devices have been demonstrated by combining semiconducting 2D materials, as optically or electronically active layers, and graphene, as transparent electrodes that allow an easy charge transfer across the interface [5–7]. In this regard, mechanically exfoliated monolayer and multilayer graphene sheets have been often proposed as electrodes in heterostructured devices to achieve higher performance compared to directly deposited metal contacts [8,9]. Integrating graphene with a proper process to minimize defects renders a high quality interface which, in turn, prevents large potential barriers between graphene and active 2D material [10,11]. Recently, mechanically exfoliated Graphene-MoS$_2$ heterostructures have been demonstrated to exhibit record responsivity and sensitivity in photodetection at room temperature as a result of efficient charge transfer [12].

However, mechanical exfoliation methods are time costly, their production yield is extremely low and the self-cleaning effect usually leads to the formation of contaminant "bubbles" under transferred crystals [1,4,6]. On the other hand, atomically sharp interfaces in Van der Waals heterostructures built up by consecutive layer-by-layer direct growth are, in practice, extremely difficult to achieve. As known, direct metal contacts growth can introduce uncontrolled defects into the 2D material, resulting in undesirable potential barrier and excessive contact resistance. Nevertheless, any industrial application will require a scalable approach so, as in the previous case of graphene and other 2D materials, techniques involving the direct growth of heterostructures as MoS$_2$/Graphene [6,13–18] and Graphene/MoS$_2$ [19–21] are being developed [22]. While graphene is a good template for direct van der Waals growth of dichalcogenides [23], the opposite is a daunting task, as the dichalcogenides suffer from stability issues [24] as previously mentioned for metals. The most typical instability mechanism is the uncontrolled formation of vacancies and S release during processing [25]. This is an important drawback as the semiconductor material in devices must preserve its functional integrity [26], and these vacancies

---

should be limited to the area just below the metal contact where the modification of the outermost layer is not critical [12]. In fact, it has been recently proposed that the controlled generation of vacancies, which leads to partial metallization, dominates the interfacial conductance, lowering potential barriers [27] or Van der Waals gaps [28]. In any case, for further scalable implementation, the metallization processes are commonly applied by patterning methods that allow local depositions [21].

In this experimental work, we present a novel approach to directly synthesize graphene films on MoS_2 at low temperature, by using plasma assisted CVD with CH_4 and H_2 as precursors. In addition, we introduce external S species, healing so the S vacancies of the dichalcogenide both of natural origin or typically induced during direct metal contact growth. Previous attempts on the direct growth of graphene on MoS_2 are scarce and mainly based on multi-step complicated protocols that result in amorphous carbon deposition. We address the direct synthesis of graphene films on an exfoliated MoS_2 single-crystal surface, following a two-step synthesis protocol to separately control the nucleation and growth stages of the film [29]. We succeeded in both increasing the grain size of graphene and improving the quality of the MoS_2 interface by adjusting processing time, temperature, precursor gases flow and partial pressures. We assess the role of H_2 flow and the influence of S vapor on the structure of the film and on the interfacial composition. Characterization experiments confirm the healing effect of S on the MoS_2 structure. The surface chemical analysis by XPS and cross-section HR-TEM morphology indicate that the formation of defects or vacancies in the MoS_2 substrate decreases when using S vapor during synthesis. Graphene conductance measurements by means of Conductive-AFM reveal that the final stoichiometry of the MoS_2 influences the conductance and this may be considered as an indirect indication of a charge transfer across the interface. The proposed low temperature growth is scalable, provides a clean and chemically controlled graphene-semiconductor interface and it is expected to have wide application on the integration of heterostructures in electronic and photonic advanced devices.

2. Experimental

2.1. Graphene synthesis

Electron Cyclotron Resonance chemical vapor deposition (ECR-CVD) plasma-assisted technique is used for the growth of graphene material from CH_4/H_2 gas mixtures. A description of the plasma CVD ASTEX AX 4500 system can be found in the SI (Fig. S1) [30]. We used as substrates few layers MoS_2 micromechanically exfoliated from single crystals (2D Semiconductors). In a series of runs, the evaporation of Sulphur powder (S) has been performed simultaneously to the graphene growth, which follows a two-steps process that differs in the H_2 pressure to control the nucleation and growth stages [29]. In the first step, high quality graphene seeds nucleate. In the second step, the growth is promoted from the nucleated dots up to the layer formation. The plasma power (200 W), temperature (650 °C), precursor (CH_4) pressure and flow, and evaporated S mass (70 mgr.) when used are kept constant throughout the study. The background pressure in routine experiments before synthesis starts is $5.4 \cdot 10^{-5}$ mbar. During graphene synthesis the total pressure is the range of $5.4 \cdot 10^{-2}$ mbar ($H_2 = 50$ sccm) and $2.2 \cdot 10^{-2}$ mbar ($H_2 = 20$ sccm). The partial pressure of CH_4 is constant in the experiments (10^{-3} mbar). We also conducted a series of experiments using acetylene as precursor (C_2H_2) and H_2 at variable flow, pressure and variable temperature range, but they lead to lower quality samples (Figs. S2–S7 in S.I).

2.2. Characterization

Room temperature atomic force microscopy (AFM) measurements are performed with a commercial instrument and software from Nanotec Electrónica S.L [35]. Two different operation modes are employed:

dynamic mode, exciting the tip at its resonance frequency (~75 kHz) to acquire topographic information of the samples, and contact mode, to sweep away the carbon deposits and measure the graphene thickness. The conductance of the continuous films is characterized by Conductive AFM (C-AFM) using a micromash HQ:NSC18/Cr-Au (Fr = 75 KHz; k = 2.8 N/m) conductive tip. The structure of our graphene films is assessed by Raman spectroscopy using a confocal Raman microscope (S&I Monovista CRS +). Raman spectra have been obtained using a 532 nm excitation laser, a 100x objective lens (NA = 0.9) and an incident laser power of 6 mW. Scanning Electron Microscopy (SEM) images are obtained with a FE-SEM FEI Nova NANOSEM 230 at low potential 5 kV to minimize electron beam induced damage. X-Ray microanalysis (EDX) spectra have been obtained using an Apollo X Silicon Drift Detector (SDD) at 15 kV potential in 20×20 μm^2 area. The chemical nature of graphene and its interface with MoS_2 is determined by X-ray Photoelectron Spectroscopy (XPS). XPS measurements are carried out under ultra-high vacuum (UHV) conditions using a PHOIBOS 100 1D delay line detector electron/ion analyzer, monochromatic Al Kα anode (1486.6 eV) and pass energy of 30 eV. The binding energy (BE) scale is calibrated with respect to the Mo 3d core level peak located at 229.2 eV [31]. All peaks presented in this work are fitted using either Voigt ("s" levels) or Doniach-Sunijch ("p" and "d" levels) functions. In all cases, the Lorentzian full-width half-maximum (FWHM-L) and the spin–orbit splitting are kept constant during the fitting (FWHM: 0.25, 0.10, and 0.15 eV for C 1s, Mo 3d, and S 2p, respectively; SO splitting: 3.12 eV and 1.18 eV for Mo 3d and S 2p, respectively), while the Gaussian width (FWHM-G) is allowed to change. For the semiquantitative analysis of the XPS areas, we carry out an internal calibration of the sensitivity factors of Mo 3d and S 2p using a pristine, freshly exfoliated MoS_2 sample (see SI for further details). High resolution Transmission Electron Microscopy HR-TEM (Scanning-STEM) cross-section images have been obtained using the aberration corrected JEOL JEM ARM200cF electronic microscope from the Spanish National Centre of Microscopy operated at 80 kV to avoid beam induced damage during observation and using a condenser lens aperture of 1 mm. The structures are resolved using an annular bright field (ABF) detector. STEM lamella samples are prepared by lift out via electron and ion milling in a Thermo Fisher DualBeam Helios NanoLab 650 focused ion beam (FIB) using a Pt protective layer.

3. Results and discussion

3.1. Growth and morphology of graphene films on MoS_2

During the experiments, we explore different H_2/CH_4 gas mixtures as the introduction of H_2 diluent is beneficial to enhance the crystallinity of the carbon material, promoting a graphitic structure [32]. Fig. 1 shows the deposition profile. The initial heating step (t_0) is carried out under an H_2 atmosphere without plasma activation in order to clean and protect the semiconducting surface. Then, we start an experimental run consisting of two growth steps. First, we nucleate graphene seeds at a given temperature T and flow ratio (H_2/CH_4) for a few minutes (t_1). Second, we vary the gas-flow by increasing the H_2/CH_4 ratio during the growth step for a given time (t_2), to enlarge the nuclei from their edges until forming a continuous film. The final cooling is also carried out under H_2 atmosphere, without plasma, to avoid graphene oxidation (t_3). During our two-step synthesis, there is a competition between the nucleation from CH_x and etching by H_x plasma species that prevent amorphous growth and stabilize the graphene. The H_2/CH_4 ratio has to be finely tuned to avoid a too high nucleation density and amorphous carbon deposition due to an excess of carbon (C) or the disappearance of the deposit or even the etching of the substrate due to a surplus of atomic hydrogen (H). We also assess the influence of using sulphur (S) during synthesis, as protecting agent for MoS_2, performing identical experiments by evaporating -or not- S powder in the reaction chamber. It is known that, in the system under study, atomic H species can interact with MoS_2 substrate inducing S-vacant formation with H_yS release
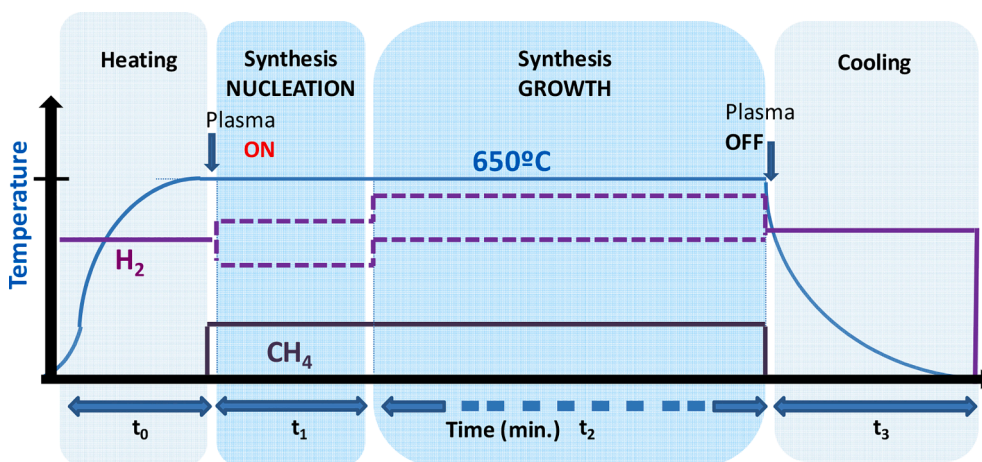
Fig. 1. Two-step synthesis. Temperature and partial pressures profile with H_2 diluent (in purple, dashed line). Temperature: 650 °C (nucleation & growth), $t_0 = 40$ min, $t_1 = 4$ min, $t_2 = 120$ min, $t_3 = 40$ min. H_2 flow is modified between 20 and 50 sccm. CH_4 flow = 2 sccm. Plasma power: 200 W.
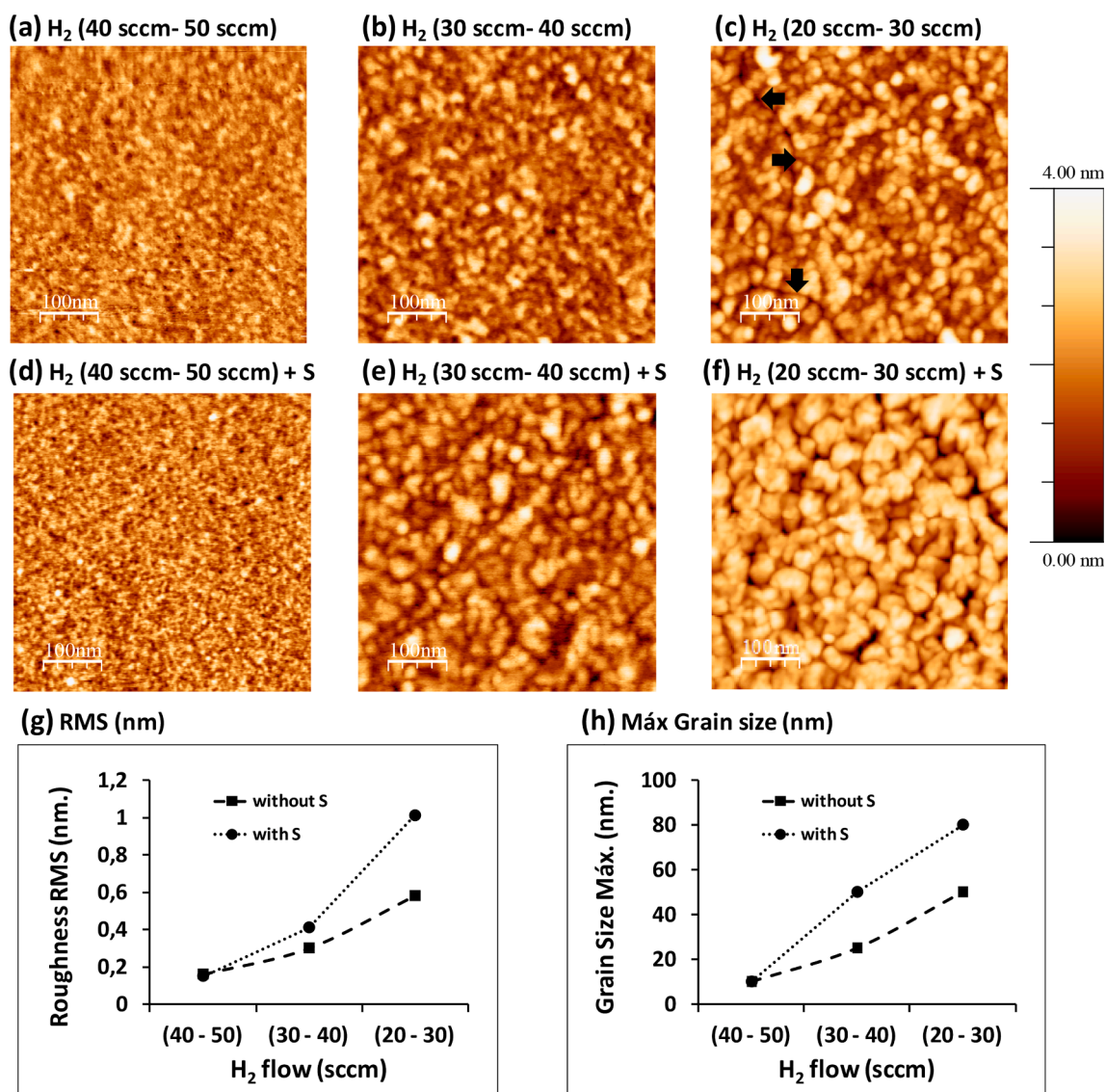

Fig. 2. (a–f) AFM topographic images of the graphene films modifying H_2 flow (top row) and including S (bottom row). The H_2 flow values indicated at the top of the images correspond to the nucleation and growth steps respectively. (g) Roughness values of the previous samples and the maximum grain size observed for each sample (h).

[33,34]. On the other hand, high quality MoS_2 films with high crystallinity and nearly perfect S/Mo ratio have been obtained after simultaneous sulfurization annealing with controlled H_2 content [33]. Processing time ($t_0 = 40$ min, $t_1 = 4$ min, $t_2 = 120$ min, $t_3 = 40$ min), plasma power: 200 W, CH_4 flow = 2 sccm, S mass = 70 mg and T are kept constant during the synthesis. Best results are achieved when a temperature of 650 °C is used during the nucleation and growth steps.

Fig. 2(a–c) shows representative AFM images of the morphology of the graphene films grown in a H_2/CH_4 atmosphere (CH_4 flow = 2 sccm) varying the flow of H_2 (H_2 flow between 20 sccm and 50 sccm) without evaporation of S. It can be observed that the grain size of the film increases as the H_2 flow decreases, from less than 10 nm in Fig. 2(a) to approximately 50 nm in Fig. 2(c). We relate this effect to an increase of the S vacancy density at the interface due to H etching of the MoS_2 substrate and presumable H_2S release [34], which in turn, promotes new nucleation points for carbon species.

Fig. 2(d–f) shows the effect of simultaneous evaporation of S in the chamber. The topographic images in Fig. 2(d–f) show that, similarly to the previous case, the grain size of the film increases and the nucleation density decreases as the H_2 flow decreases. However, the addition of S is critical, as it can be seen compeering both images, the average grain size doubles its size, from about 10 nm in Fig. 2(d) to more than 80 nm in Fig. 2(f). This difference in grain size is more difficult to observe when the H_2 flow is very high, Fig. 2(a) and (d) but the effect is enhanced for lower H_2 flow (see Fig. 2(c) and (f)). We attribute this effect to the competition between the healing effect of S atoms and the spallation effect induced by the H species from the plasma. A concomitant effect of the grain size enhancement that we compile in Fig. 2(h) is the roughness (RMS) increase, Fig. 2(g). As the H_2 flow decreases the RMS (nm) increases regularly and this effect is pronounced with S addition, directly related to the grain size.

These results point out that the S/H ratio is a critical factor to take into account in order to apply this strategy for further optimization of the growth, as previously observed in dichalcogenides synthesis [33]. If less S or more H is used, the beneficial effect is hardly observed or it does not exist. However, as the contribution of H_2 is essential to graphitize the carbon deposit, if we decrease the H_2 flow below the displayed values in Fig. 2 (from 20 sccm to 50 sccm) the deposit loses its crystallinity [32]. On the other hand, if we increase the H_2 flow above, the substrate is heavily etched. In fact, a close observation of Fig. 2(c) reveals the existence of cracks on the surface (black arrows). In order to check if this effect also occurs in other cases, we explore the samples at low magnification by AFM (see Fig. S8) and SEM. Fig. 3(a) shows the SEM image of the morphology of the sample grown without S, previously discussed in Fig. 2(c), where it can be clearly observed the existence of cracks regularly distributed over the entire surface. This effect, also observed in Fig. S8, confirms the instability of the sample and the release of S atoms. The etching of Mo atoms cannot be ruled out. Fig. 3(b) shows the morphology of the sample grown with S where no cracks appear. It can be also observed the granular morphology of the graphene film. Finally we include in Fig. 3(c) the SEM image of the planar surface of freshly exfoliated pristine MoS_2 as a comparison, where flat morphology is only observed due to the atomic van der Waals surface of the sample. We also analyse the samples inside the SEM by EDX in order to detect
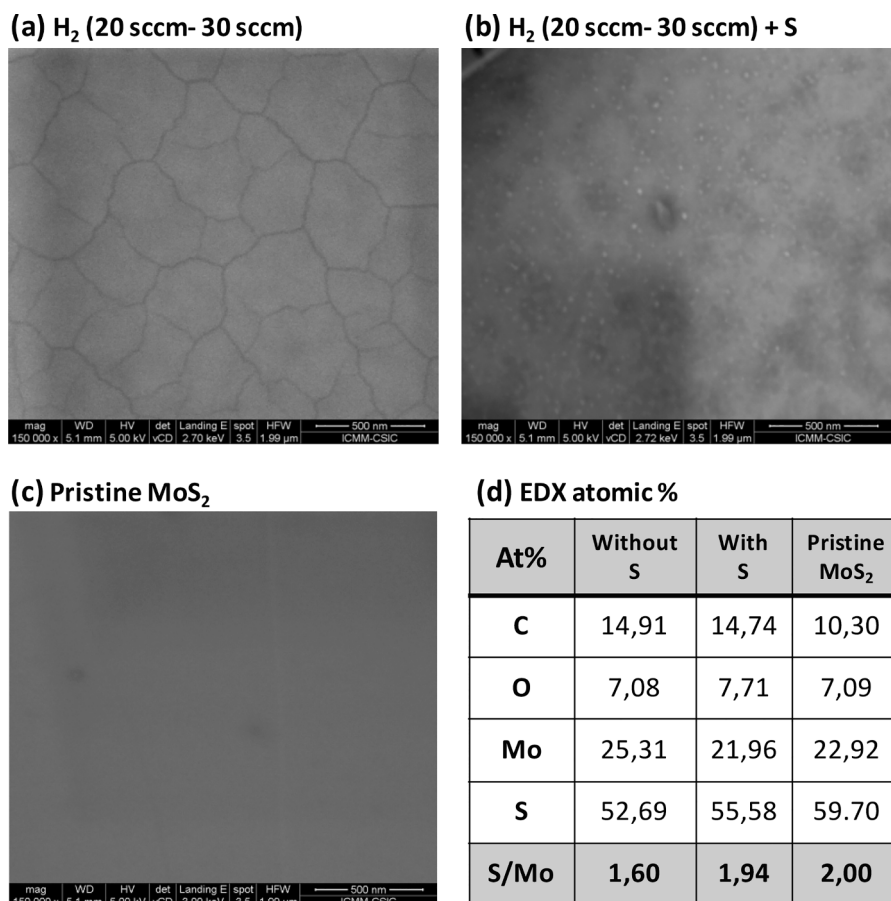
(a) H$_2$ (20 sccm- 30 sccm)

(b) H$_2$ (20 sccm- 30 sccm) + S

(c) Pristine MoS$_2$

(d) EDX atomic %

At%	Without S	With S	Pristine MoS$_2$
C	14,91	14,74	10,30
O	7,08	7,71	7,09
Mo	25,31	21,96	22,92
S	52,69	55,58	59.70
S/Mo	1,60	1,94	2,00

Fig. 3. SEM images of the graphene films grown without S (a), with S (b) and pristine MoS_2 topography (c). (d) EDX% atomic semiquantitative analysis of the previous samples. We include the C, O, Mo, S in the quantitative analysis and normalize the S/Mo ratio = 2 with the values obtained in the pristine MoS_2 single crystal as a standard.

compositional differences between them (see section S1 in S.I.). Fig. 3(d) presents the semi-quantitative analysis of the three samples. We can observe that, along with the expected signals of C, Mo and S, we detect O of environmental origin in our samples in similar amounts. The C signal is also detected in the pristine sample that is also related to environmental contamination. The C signal in the grown samples appears in similar atomic quantities, 14.91% for the sample grown without S and 14.74% in the sample grown with S. This result is in good agreement with the fact that the all the synthesis parameters are similar in both samples except S addition and the samples have comparable thicknesses. In order to understand the values obtained for the Mo and S, we use the S/Mo ratio. After normalization of the values, taking into account that in the pristine sample the S/Mo ratio = 2, the results clearly show that a high amount of S is removed from the sample grown without S during synthesis with a final S/Mo = 1.60. However, the sample grown with S exhibits an S/Mo = 1.94, apparently proving the healing effect of the additional S atoms. It should be carefully considered here that the EDX analysis also provides information from the bulk of the samples and this analysis must be completed with surface sensitive and high resolution techniques that we include in the following section. In this point we can conclude that the introduction of a large amount of S during the synthesis enables the increase of the grain size of the graphene films, decreasing the activation of the substrate by H species and minimizing the nucleation points.

3.2. Structural characterization of graphene films and interface analysis

Fig. 4(a) shows a representative Raman spectrum of each sample shown in Fig. 2 (see the five point Raman analyses for each sample in Fig. S9). All spectra clearly exhibit the typical D, G and 2D carbon bands, confirming the graphenic nature of the films. In our nanocrystalline graphitic samples the physical meaning of the I_D/I_G ratio values is related both to film grain size and functionalization with remaining hydrogen. It is known that in nanocrystalline samples I_D/I_G varies inversely with the crystal size being the grain boundaries the main contribution to defect related peak I_D. Hydrogenation could also contribute to I_D due to the formation of C—H sp^3 bonds as well as the breaking of the translational symmetry of C=C sp^2 bonds being this effect more pronounced in samples growth with high H_2 pressure [35,36]. Fig. 4(b) shows the I_D/I_G ratio of the corresponding samples in Fig. 4(a) and Fig. S9. It is noted that as the H_2 flow decreases, so does the I_D/I_G ratio that varies from $I_D/I_G \sim 3$ to $I_D/I_G \sim 2$ when S is not evaporated. However, this effect is even more pronounced when using S, changing from $I_D/I_G \sim 3$ to $I_D/I_G \sim 1.2$. This observation is in good agreement with the grain size previously discussed in Fig. 2. As the grain size increases -and the H_2 flow decreases-, the peak I_D/I_G ratio decreases, being the grain boundaries the main contribution to the Raman D peak. Fig. 4(c) depicts the evolution of the I_{2D}/I_G peak ratio of the corresponding Raman spectra. It is known that 2D peak is the overtone of the D peak but, unlike the D peak, it does not need defects for its activation and it is thus always present in graphitic samples with suitable quality. Indeed the 2D intensity and width is directly related to the film quality in monolayer graphene samples and also the I_{2D}/I_G peak ratio is related to the film thickness in few layer graphene [35]. The I_{2D}/I_G values in Fig. 4(c) show noticeable variation comparing different samples, with I_{2D}/I_G ratios between 0.4 and 0.6, indicating formation of few layers thickness graphene (around 2–3 nm, see section S2 and Fig. S10 in S.I.). However, it can be observed that the I_{2D}/I_G ratio decreases both as we decrease the hydrogen and without S content. This gradual reduction with H_2 in our samples is directly related to a slight increase on film thickness perceived through the roughness analysis depicted previously in Fig. 2(g–h). Moreover we guess that the I_{2D}/I_G ratio increase with S addition is related to a higher quality films owing to a grain size enhancement.

Fig. 5(a) and (b) shows high resolution AFM topographic images of graphene films deposited with low H_2 flow (20 sccm in the nucleation step − 30 sccm in the growth step), without and with S evaporation, respectively. Sample grown with S (panel b) not only evidences larger grain size but also well-defined hexagonal crystals with parallel edges that unambiguously confirm the few layer graphene deposition on MoS_2.

After the structural characterization of the films, we address the interface analysis between the graphene film and MoS_2 substrate and the exploration of the cross-section morphology of the heterostructure. Fig. 5(c) shows the characteristic XPS C 1s core level spectra obtained
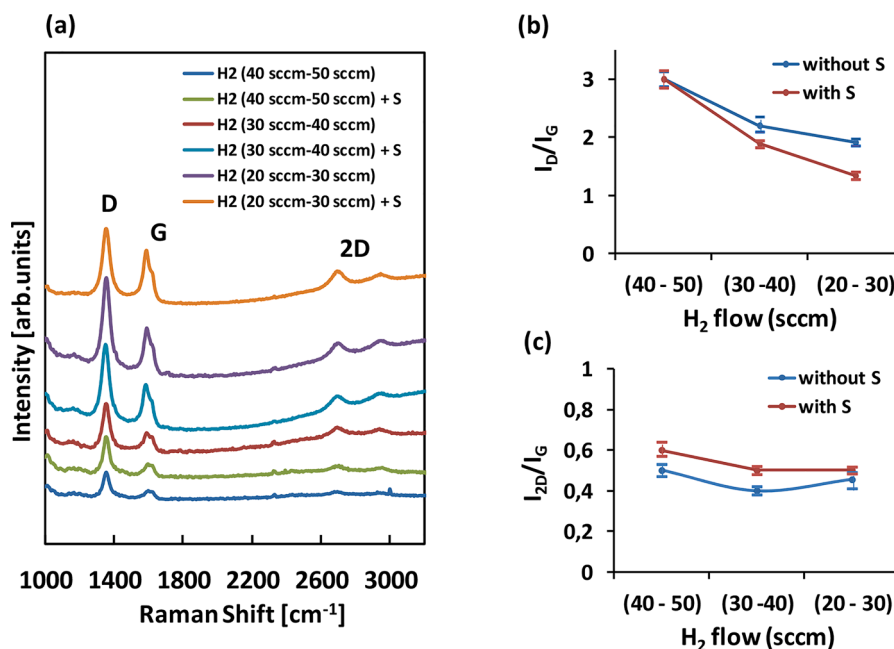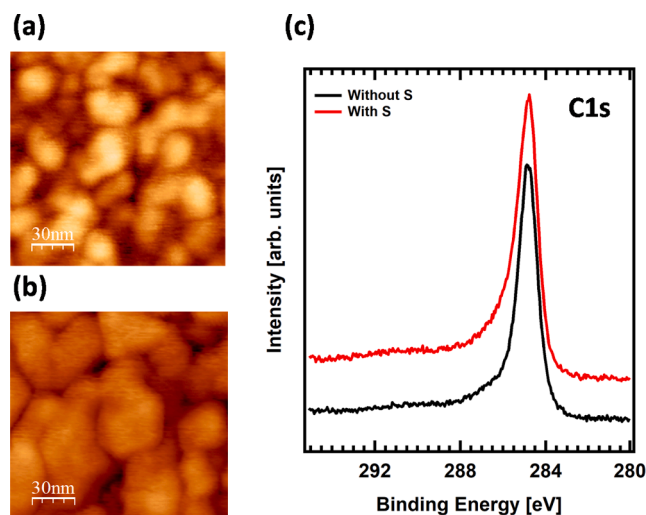

Fig. 4. (a) Confocal Raman spectra of the samples comparing different H_2 flows with and without introduction of S. (b) I_D/I_G ratio of spectra in panel (a) and Fig. S9 including the error bars. (c) I_{2D}/I_G ratio of spectra in panel (a) and Fig. S10 including the error bar for each point.

(a)

(b)

(c)

Fig. 5. (a, b) High resolution AFM topographic image of the samples deposited with H_2 flow (20 sccm- 30 sccm) without (a) and with S (b). (c) XPS C 1s core level spectra of the samples deposited in two steps with H_2 flow (20 sccm-30 sccm) without S (black line) and with S (red line). (For interpretation of the references to colour in this figure legend, the reader is referred to the web version of this article.)

from both samples, grown with and without S evaporation (red and black curves, respectively). We notice the comparable intensity of the carbon signal of both spectra, an indication of similar thickness. Moreover, in both cases, the signal presents a main component at 284.7 eV, characteristic of a sp^2 configuration and thus, compatible with the presence of graphene [37–39]. Other contributions associated with C—O or C—OH species, which could be due to functionalization of the grain boundaries or to interfacial chemical states such as carbide formation (Mo—C at 283.3 eV, S—C bonds at 284.1 eV) are not clearly observed, although they cannot be ruled out with certitude as their intensity can be very weak [21].

In order to further elucidate the chemical structure and quality of the interface between graphene and MoS_2, we analyse the Mo 3d and S 2p XPS core level spectra associated to samples deposited with a H_2 flow (20 sccm- 30 sccm), with and without S including a semi-quantitative analysis in order to obtain an approximation of the elemental interfacial composition. We also perform HR-TEM cross-section morphology analysis of two samples grown with and without S. Fig. 6 presents the characteristic XPS Mo 3d and S 2p core level spectra and the HR-TEM cross-section images. The Mo 3d peak in Fig. 6(a) shows two components corresponding to the Mo 3d5/2 (229.1 eV) and 3d3/2 (232.3 eV) core levels of pure MoS_2. Comparing the spectra of both samples, with (red line) and without S (black line), no clear difference in position or shape of any of those peaks is observed. In the same way, the S 2p core level in Fig. 6(b) shows the typical S 2p3/2 (162.0 eV) and S 2p1/2 (163.2 eV) doublet of MoS_2.

Other contributions due to interfacial chemical bonds with graphene such as carbide formation (Mo—C at 231.3 eV or S—C bonds at 162.5 eV), or Mo—S (peaks at 228.9 eV and 163.5 eV) are not observed. Nevertheless, a semi-quantitative analysis of the samples shows a clear compositional difference at the interface. Results clearly confirm that both samples experience S vacancy formation during synthesis. However, the S release is significantly higher (~12%) from the sample where no S is added during the growth (S/Mo = 1.56) in comparison with the

other sample deposited with S (S/Mo = 1.81) (see section S3, in S.I). These values indicate that the new evaporated S species are being included in the TMD structure, healing defects. Putting together these XPS results with the previous EDX analysis in Fig. 3, we can conclude that the sample grown without S suffers from S release from surface and bulk in similar quantities (XPS S/Mo = 1.56 and EDX S/Mo = 1.60). However the sample grown with S undergoes S release more confined to its first layers (XPS S/Mo = 1.81 and EDX S/Mo = 1.94). In the case of compensation with S, the S/Mo ratio is 1.81 where ideally it should be 2, highlighting the fact that the amount of evaporated S during growth does not fully recover the atomic S release from the sample. Moreover, the EDX and XPS results demonstrate that there exists S release from the subsurface layers that is even more difficult to retrieve. Fig. 6(c) and (d) show the HRTEM images in cross-section for both samples grown without and with S respectively. The more important aspect of the images is the interfacial contact morphology between the graphitic layer and the MoS_2 substrate. It can be clearly observed that in Fig. 6(c) from the sample grown without S the interface is not abrupt and the junction is progressively formed between both materials. Moreover, the junction is not atomically flat as the dashed black line in the image shows. The resolution could be also limited by the loss of crystallinity and the accumulation of defects. Fig. 6(d) shows a different situation in the sample grown with S. The interface is extremely sharp and abrupt and the junction is atomically flat as the dotted black line indicates. The single crystal MoS_2 substrate is observed with nearly atomic resolution. However, the graphene planes are not clearly observed most probably due to the nanocrystalline character of the film, being the average grain size smaller than the sample lamella thickness. There is no clear evidence of defects in MoS_2, however the existence of atomic S vacancies in the first MoS_2 layers cannot be completely ruled out, even more taking into account the XPS analysis. This results overall unambiguously show the critical role played by additional S in the stoichiometry of the MoS_2 surface and therefore, the addition of S during the plasma growth clearly reduces the amount of S vacancies, i.e. nucleation sites.

3.3. Electrical characterization of graphene films

In order to obtain comparative information on the electrical performance and conductivity of the graphene films grown with and without S evaporation, we record the electrical characteristics in a two-terminal configuration by means of conductive atomic force microscopy (C-AFM), which is an appealing lithography-free option [40,41]. Fig. 7(a) depicts the schematic representation of the C-AFM configuration used to accomplish the measurements. We use Ag as a macroscopic metal contact and the Au coated AFM tip as the opposite nano-contact. To assess the resistivity, we measure the current–voltage characteristics of the film and the variation of the resistance while modifying the distance (d) between the two contacts, by moving the AFM tip. In this way, we greatly eliminate the contribution of eventual contact resistances, for example at the nano-tip side. The initial distance between contacts (d_0) is typically between 0.2 mm and 0.4 mm and it depends on the exfoliated sample size and morphology. Sample morphology sometimes presents folds or wrinkles conditioning the initial distance (d_0).

Then, we move the tip away measuring the resistance at other points up to a distance of 80 μm from the initial point d_0. At each intermediate point, we performed up to five I-V curves from which the resistance value is obtained (see Fig. S11 that presents average values obtained at the initial distance d_0). Fig. 7 (b) shows the resistance ΔR (kΩ) extracted from the slope of a linear fit to the I-Vs recorded as a function of distance (d) from two samples grown with medium (30–40 sccm) H_2 flow, with S
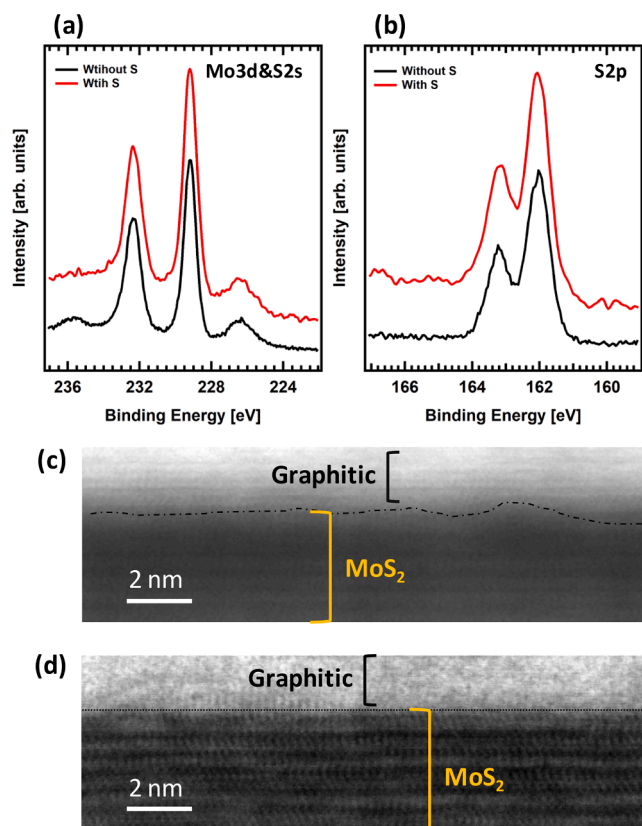
Fig. 6. High resolution XPS spectra of the samples deposited in two steps with H_2 flow (20–30 sccm) without S (black line) and with S (red line). (a) Mo 3d core level peaks. (b) S 2p core level peaks. HR-TEM cross-section analysis of the samples grown without S (c) and with S (d). (For interpretation of the references to colour in this figure legend, the reader is referred to the web version of this article.)

(top panel) and without S (bottom panel). The linear fit seems to be correctly applied in the sample grown without S. However some discrepancy is observed between the fit and the data plotted for the other sample. We ascribe this effect to the different grain size and roughness discussed in Fig. 2 that modify more notably the tip contact area (R^C_{Au-Gr} in Fig. 8(a)) in the sample grown with S. Anyway, we accept the fit for comparative purposes. Fig. 7(b) clearly shows that the resistance of the film is larger when S is added. This can be rationalized considering the

influence in the conductance that the degree of reduction of MoS_2, observed in XPS semiquantitative analyses, may have. As the S/Mo ratio decreases, the metallization degree of MoS_2 increases and this could affect the final conductance of the graphene film due to a charge transfer effect between both materials, effectively electronically doping the top graphene film, or due to the reduction of resistance both on the MoS_2 itself (n-doping effect) and on the graphene-MoS_2 interface (R^S_{MoS2} and $R^C_{Gr-MoS2}$ in the electrical model of our system, Fig. 8(a)) [27].

We believe that the first charge transfer effect is dominant in this case and that the second effect does not play an important role in the final measured resistivity, whose equivalent circuit is depicted in Fig. 8(a). In order to further clarify this point, Fig. 7(c) shows the C-AFM I/V characteristics of a pristine MoS_2 sample in comparison with a MoS_2 sample treated with H_2 plasma. The asymmetry in the I-V curves is due to the difference between the work functions of Ag and Au, which give effectively a Schottky diode configuration (the contact between MoS_2 and Ag is expected to be Ohmic, while Au-MoS_2 gives a rectifying contact, see Fig. 8(b)). In these I-Vs, the slope of the current versus at large positive voltages (forward bias) gives the value of the series resistance, which in this case is dominated by the MoS_2 sheet resistance R^S_{MoS2} (see equivalent circuit in Fig. 8(b)). After H_2 treatment, the MoS_2 sheet conductance shows an overall increase (red line in Fig. 7(c)). Despite this increase, the value of sheet resistance that we observe in the MoS_2 is approximately three orders of magnitude larger (R ≈ 2.0 MΩ, see Fig. 9) than the resistance of the graphene films estimated in Fig. 7(b) (ΔR in kΩ range), thus justifying the assumption that we are mostly sensitive to the sheet resistance of the electronically doped graphene films (see the equivalent circuit in Fig. 8(a)).

As the film grown without S presents higher doping level, this fact probably counteracts the effect that the grain size increase, observed when growing with S, could have in the conductance enhancement. In order to extract more quantitative information about the film conductivity and, more specifically, about the potential barrier at the contacts, we perform a fit to the curves in Fig. 7(c) using the Shockley diode equation with a series resistance that represents the contribution from R^S_{MoS2} (see S4, Figs. 8 and 9). From this fit, we estimate that the difference between the Schottky barriers in the pristine and reduced cases is $\Phi_{pristine} - \Phi_{reduced} = 15$ meV. This reduction trend in the Schottky barrier height observed in the Au-MoS_2 system is also expected to occur, with the corresponding magnitude, in the graphene-MoS_2 interface. In fact, localized S vacancies in 2D dichalcogenides under the metal contact have been proposed as the main reason for the increase of current through the metal–semiconductor heterojunctions, including Schottky barrier reduction that is in good agreement with our last experiments [27]. These results agree also with recent studies on artificially induced
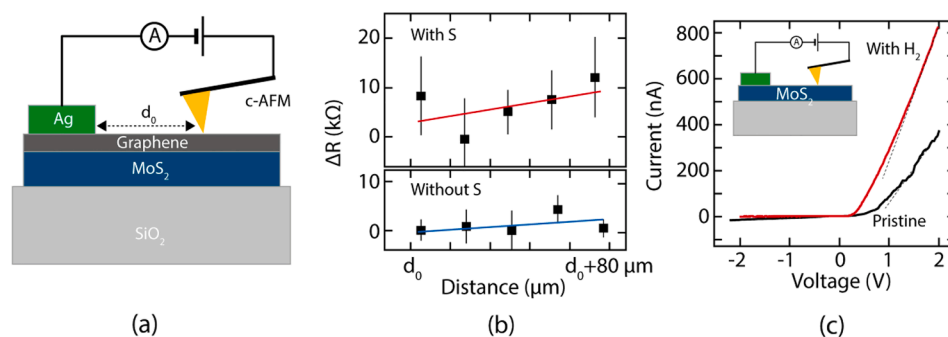
Fig. 7. (a) C-AFM I-V measurement set-up. Contact distance d is variable between 0.2 and 0.4 mm depending on the sample in an initial point d_0. Then it is increased up to a distance of 80 μm. (b) Resistance variation (kΩ) as a function of distance (d), $d_0 = 0.2$–0.4 mm corresponds to 0 point distance in these curves. Linear fit (red line slope = 0.046, blue line slope = 0,025). (c) C-AFM I-V characteristics of a pristine and reduced MoS_2. (For interpretation of the references to colour in this figure legend, the reader is referred to the web version of this article.)
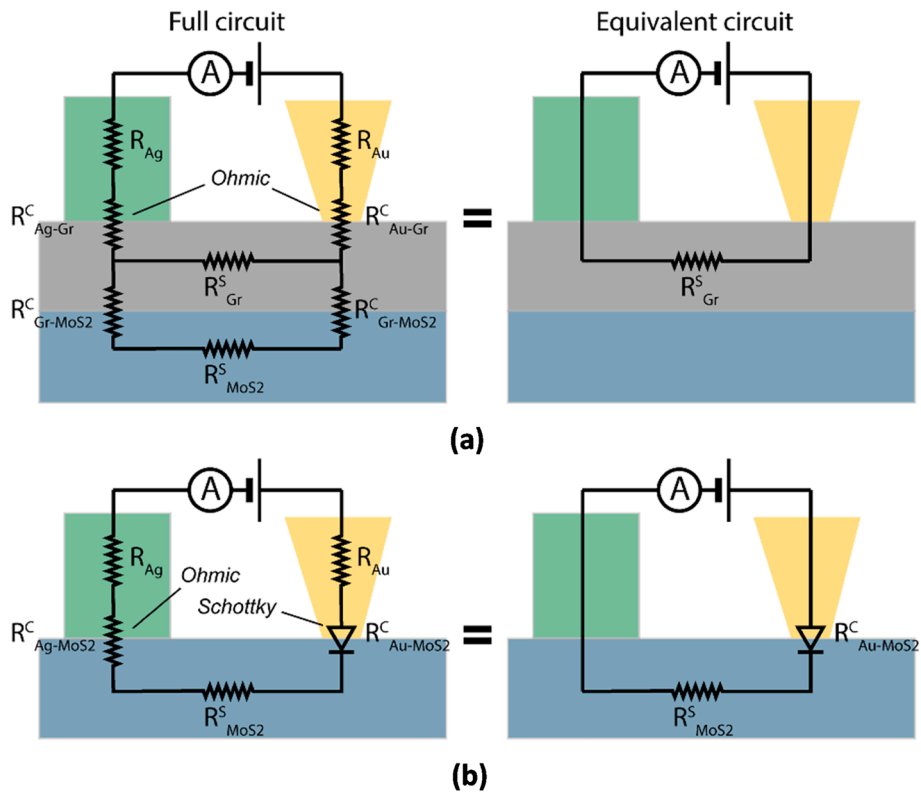
Fig. 8. Electrical model of the C-AFM set-up, including graphene-MoS$_2$ heterostructure (a) and MoS$_2$ on SiO$_2$ (b). (a) R$_{Ag}$ = resistance of Ag; R$^C_{Ag-Gr}$ = contact resistance between graphene and Ag; R$_{Au}$ = resistance of the Au coated AFM tip; R$^C_{Au-Gr}$ = contact resistance between graphene and the Au tip contact [40,42]; R$^S_{Gr}$ = sheet resistance of graphene; R$^S_{MoS2}$ = sheet resistance of MoS$_2$; R$^C_{Gr-MoS2}$ = contact resistance between graphene and MoS$_2$. (b) R$^C_{Ag-MoS2}$ = contact resistance between MoS$_2$ and Ag; R$^C_{Au-MoS2}$ = contact resistance between MoS$_2$ and the Au tip contact.

S vacancies on transition metal dichalcogenides by hydrogen annealing that have been demonstrated to be a universal strategy to eliminate the vdW gap in semiconducting heterostructures [28]. Accordingly, our healing strategy to minorize S vacancies by evaporating S powder while growing is efficient and can be easily implemented in the direct growth protocols. With the introduction of S, a balance between the healing effect of evaporated S atoms and the reduction mechanism of H species from de plasma is achieved leading to high quality graphene deposits on MoS$_2$ with tailored interface.

4. Conclusions

The present study demonstrates an efficient methodology for the direct growth of graphene on MoS$_2$, suitable for heterostructure synthesis. The structure of the graphene films grown and the chemistry at its interface with MoS$_2$ can be tailored modifying the synthesis parameters. On one hand, the H$_2$/CH$_4$ ratio and S/H ratio have to be finely tuned to achieve graphene grain sizes surpassing ~80 nm. On the other hand, S/H ratio is critical to tailor the interfacial composition. The EDX and XPS analyses show that S vacancies formation dynamics is minimized by simultaneous evaporation of S from powder during synthesis. Moreover, C-AFM electrical measurements indicate that the conductance of the
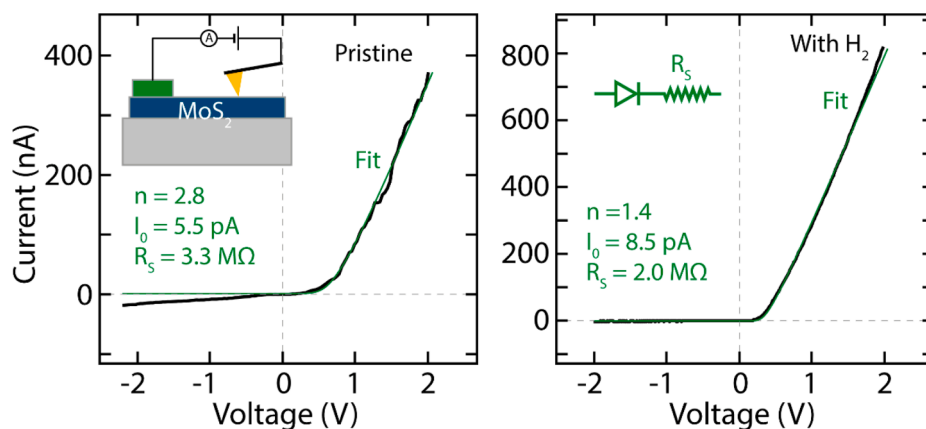
Fig. 9. C-AFM I-V characteristics of pristine (left) and reduced (right) MoS$_2$. The green line is a fit to the diode model with a series resistance. n corresponds to ideality factor [11]. I$_0$ is the diode saturation current.

films and the graphene-MoS$_2$ junctions are influenced by the formation of interfacial vacancies. In conclusion, after analyzing the results observed in our experiments, our strategy can be understood as a means to tailor the stoichiometry and contact resistance of the directly grown metal–semiconductor junction without disturbing the active semiconducting material. The reported processes are intrinsically clean and scalable and can be applied onto other semiconducting heterostructures.

CRediT authorship contribution statement

Roberto Muñoz: Conceptualization, Methodology, Validation, Formal analysis, Investigation, Resources, Writing – original draft, Writing – review & editing. **Elena López-Elvira:** Investigation, Formal analysis, Writing – review & editing. **Carmen Munuera:** Investigation, Formal analysis, Resources, Writing – review & editing. **Riccardo Frisenda:** Formal analysis, Writing – review & editing. **Carlos Sánchez-Sánchez:** Resources, Investigation, Formal analysis, Writing – review & editing. **José Ángel Martín-Gago:** Resources, Writing – review & editing. **Mar García-Hernández:** Conceptualization, Resources, Writing – review & editing, Funding acquisition, Project administration.

Declaration of Competing Interest

The authors declare that they have no known competing financial interests or personal relationships that could have appeared to influence the work reported in this paper.

Acknowledgements

Appendix A. Supplementary material

Supplementary data to this article can be found online at https://doi.org/10.1016/j.apsusc.2021.151858.

References

[1] A.K. Geim, I.V. Grigorieva, Van der Waals heterostructures, Nature 499 (7459) (2013) 419–425.

[2] A. Castellanos-Gomez, M. Buscema, R. Molenaar, V. Singh, L. Janssen, H.S.J. van der Zant, G.A. Steele, Deterministic transfer of two-dimensional materials by all-dry viscoelastic stamping, 2D Mater. 1 (2014), 011002.

[3] R. Frisenda, E. Navarro-Moratalla, P. Gant, D. Pérez De Lara, P. Jarillo-Herrero, R.V. Gorbachev, A. Castellanos-Gomez, Recent progress in the assembly of nanodevices and van der Waals heterostructures by deterministic placement of 2D materials, Chem. Soc. Rev. 47 (1) (2018) 53–68.

[4] A.V. Kretinin, Y. Cao, J.S. Tu, G.L. Yu, R. Jalil, K.S. Novoselov, S.J. Haigh, A. Gholinia, A. Mishchenko, M. Lozada, T. Georgiou, C.R. Woods, F. Withers, P. Blake, G. Eda, A. Wirsig, C. Hucho, K. Watanabe, T. Taniguchi, A.K. Geim, R. V. Gorbachev, Electronic Properties of Graphene Encapsulated with Different Two-Dimensional Atomic Crystals, Nano Lett. 14 (6) (2014) 3270–3276.

[5] L. Britnell, R.M. Ribeiro, A. Eckmann, R. Jalil, B.D. Belle, A. Mishchenko, Y.-J. Kim, R.V. Gorbachev, T. Georgiou, S.V. Morozov, A.N. Grigorenko, A.K. Geim, C. Casiraghi, A.H.C. Neto, K.S. Novoselov, Strong Light-Matter Interactions in Heterostructures of Atomically Thin Films, Science 340 (6138) (2013) 1311–1314.

[6] K.S. Novoselov, A. Mishchenko, A. Carvalho, A.H. Castro Neto, 2D materials and van der Waals heterostructures, Science 353 (6298) (2016) aac9439.

[7] S. Bertolazzi, D. Krasnozhon, A. Kis, Nonvolatile Memory Cells Based on MoS2/Graphene Heterostructures, ACS Nano 7 (4) (2013) 3246–3252.

[8] W.S. Leong, X. Luo, Y. Li, K.H. Khoo, S.Y. Quek, J.T.L. Thong, Low Resistance Metal Contacts to MoS2 Devices with Nickel-Etched-Graphene Electrodes, ACS Nano 9 (1) (2015) 869–877.

[9] W.S. Leong, H. Gong, J.T.L. Thong, Low-Contact-Resistance Graphene Devices with Nickel-Etched-Graphene Contacts, ACS Nano 8 (1) (2014) 994–1001.

[10] H. Li, J.-B. Wu, F. Ran, M.-L. Lin, X.-L. Liu, Y. Zhao, X. Lu, Q. Xiong, J. Zhang, W. Huang, H. Zhang, P.-H. Tan, Interfacial Interactions in van der Waals Heterostructures of MoS2 and Graphene, ACS Nano 11 (11) (2017) 11714–11723.

[11] Q. Zhao, W. Jie, T. Wang, A. Castellanos-Gomez, R. Frisenda, InSe Schottky Diodes Based on Van Der Waals Contacts, Adv. Funct. Mater. 30 (2020) 2001307.

[12] K. Roy, M. Padmanabhan, S. Goswami, T.P. Sai, G. Ramalingam, S. Raghavan, A. Ghosh, Graphene–MoS2 hybrid structures for multifunctional photoresponsive memory devices, Nat. Nanotechnol. 8 (11) (2013) 826–830.

[13] J.A. Miwa, M. Dendzik, S.S. Grønborg, M. Bianchi, J.V. Lauritsen, P. Hofmann, S. Ulstrup, Van der Waals Epitaxy of Two-Dimensional MoS2–Graphene Heterostructures in Ultrahigh Vacuum, ACS Nano 9 (6) (2015) 6502–6510.

[14] Y. Shi, W.u. Zhou, A.-Y. Lu, W. Fang, Y.-H. Lee, A.L. Hsu, S.M. Kim, K.K. Kim, H. Y. Yang, L.-J. Li, J.-C. Idrobo, J. Kong, van der Waals Epitaxy of MoS2 Layers Using Graphene As Growth Templates, Nano Lett. 12 (6) (2012) 2784–2791.

[15] Y.-C. Lin, N. Lu, N. Perea-Lopez, J. Li, Z. Lin, X. Peng, C.H. Lee, C.e. Sun, L. Calderin, P.N. Browning, M.S. Bresnehan, M.J. Kim, T.S. Mayer, M. Terrones, J. A. Robinson, Direct Synthesis of van der Waals Solids, ACS Nano 8 (4) (2014) 3715–3723.

[16] L. Yu, Y.-H. Lee, X.i. Ling, E.J.G. Santos, Y.C. Shin, Y. Lin, M. Dubey, E. Kaxiras, J. Kong, H. Wang, T. Palacios, Graphene/MoS2 Hybrid Technology for Large-Scale Two-Dimensional Electronics, Nano Lett. 14 (6) (2014) 3055–3063.

[17] Y. Kim, D. Choi, W.J. Woo, J.B. Lee, G.H. Ryu, J.H. Lim, S. Lee, Z. Lee, S. Im, J.-H. Ahn, W.-H. Kim, J. Park, H. Kim, Synthesis of two-dimensional MoS2/graphene heterostructure by atomic layer deposition using MoF6 precursor, Appl. Surf. Sci. 494 (2019) 591–599.

[18] H.-U. Kim, M. Kim, Y. Jin, Y. Hyeon, K.S. Kim, B.-S. An, C.-W. Yang, V. Kanade, J.-Y. Moon, G.Y. Yeom, D. Whang, J.-H. Lee, T. Kim, Low-temperature wafer-scale growth of MoS2-graphene heterostructures, Appl. Surf. Sci. 470 (2019) 129–134.

[19] W. Fu, F.-H. Du, J. Su, X.-H. Li, X. Wei, T.-N. Ye, K.-X. Wang, J.-S. Chen, In situ catalytic growth of large-area multilayered graphene/MoS2 heterostructures, Sci. Rep. 4 (2014) 4673.

[20] W. Kwieciński, K. Sotthewes, B. Poelsema, H.J.W. Zandvliet, P. Bampoulis, Chemical vapor deposition growth of bilayer graphene in between molybdenum disulfide sheets, J. Colloid Interface Sci. 505 (2017) 776–782.

[21] E. Lee, S.G. Lee, W.H. Lee, H.C. Lee, N.N. Nguyen, M.S. Yoo, K. Cho, Direct CVD Growth of a Graphene/MoS2 Heterostructure with Interfacial Bonding for Two-Dimensional Electronics, Chem. Mater. 32 (11) (2020) 4544–4552.

[22] C. Backes, A.M. Abdelkader, C. Alonso, A. Andrieux-Ledier, R. Arenal, J. Azpeitia, N. Balakrishnan, L. Banszerus, J. Barjon, R. Bartali, S. Bellani, C. Berger, R. Berger, M.M.B. Ortega, C. Bernard, P.H. Beton, A. Beyer, A. Bianco, P. Bøggild, F. Bonaccorso, G.B. Barin, C. Botas, R.A. Bueno, D. Carriazo, A. Castellanos-Gomez, M. Christian, A. Ciesielski, T. Ciuk, M.T. Cole, J. Coleman, C. Coletti, L. Crema, H. Cun, D. Dasler, D. De Fazio, N. Díez, S. Drieschner, G.S. Duesberg, R. Fasel, X. Feng, A. Fina, S. Forti, C. Galiotis, G. Garberoglio, J.M. García, J.A. Garrido, M. Gibertini, A. Gölzhäuser, J. Gómez, T. Greber, F. Hauke, A. Hemmi, I. Hernandez-Rodriguez, A. Hirsch, S.A. Hodge, Y. Huttel, P.U. Jepsen, I. Jimenez, U. Kaiser, T. Kaplas, H. Kim, A. Kis, K. Papagelis, K. Kostarelos, A. Krajewska, K. Lee, C. Li, H. Lipsanen, A. Liscio, M.R. Lohe, A. Loiseau, L. Lombardi, M. Francisca López, O. Martin, C. Martín, L. Martínez, J.A. Martin-Gago, J. Ignacio Martínez, N. Marzari, Á. Mayoral, J. McManus, M. Melucci, J. Méndez, C. Merino, P. Merino, A.P. Meyer, E. Miniussi, V. Miseikis, N. Mishra, V. Morandi, C. Munuera, R. Muñoz, H. Nolan, L. Ortolani, A.K. Ott, I. Palacio, V. Palermo, J. Parthenios, I. Pasternak, A. Patane, M. Prato, H. Prevost, V. Prudkovskiy, N. Pugno, T. Rojo, A. Rossi, P. Ruffieux, P. Samorì, L. Schué, E. Setijadi, T. Seyller, G. Speranza, C. Stampfer, I. Stenger, W. Strupinski, Y. Svirko, S. Taioli, K.B.K. Teo, M. Testi, F. Tomarchio, M. Tortello, E. Treossi, A. Turchanin, E. Vazquez, E. Villaro, P. R. Whelan, Z. Xia, R. Yakimova, S. Yang, G.R. Yazdi, C. Yim, D. Yoon, X. Zhang, X. Zhuang, L. Colombo, A.C. Ferrari, M. Garcia-Hernandez, Production and processing of graphene and related materials, 2D Mater. 7 (2020), 022001.

[23] A. Azizi, S. Eichfeld, G. Geschwind, K. Zhang, B. Jiang, D. Mukherjee, L. Hossain, A. F. Piasecki, B. Kabius, J.A. Robinson, N. Alem, Freestanding van der Waals Heterostructures of Graphene and Transition Metal Dichalcogenides, ACS Nano 9 (5) (2015) 4882–4890.

[24] Y. Guo, D. Liu, J. Robertson, Chalcogen vacancies in monolayer transition metal dichalcogenides and Fermi level pinning at contacts, Appl. Phys. Lett. 106 (2015), 173106.

[25] D. Liu, Y. Guo, L. Fang, J. Robertson, Sulfur vacancies in monolayer MoS2 and its electrical contacts, Appl. Phys. Lett. 103 (2013), 183113.

[26] A. Allain, J. Kang, K. Banerjee, A. Kis, Electrical contacts to two-dimensional semiconductors, Nat. Mater. 14 (12) (2015) 1195–1205.

[27] S. McDonnell, R. Addou, C. Buie, R.M. Wallace, C.L. Hinkle, Defect-Dominated Doping and Contact Resistance in MoS2, ACS Nano 8 (3) (2014) 2880–2888.

[28] Y. Wen, P. He, Y. Yao, Y. Zhang, R. Cheng, L. Yin, N. Li, J. Li, J. Wang, Z. Wang, C. Liu, X. Fang, C. Jiang, Z. Wei, J. He, Bridging the van der Waals Interface for Advanced Optoelectronic Devices, Adv. Mater. 32 (2020) 1906874.

[29] R. Muñoz, C. Munuera, J.I. Martínez, J. Azpeitia, C. Gómez-Aleixandre, M. García-Hernández, Low temperature metal free growth of graphene on insulating substrates by plasma assisted chemical vapor deposition, 2D Mater. 4 (2016), 015009.

[30] R. Muñoz, C. Gómez-Aleixandre, Fast and non-catalytic growth of transparent and conductive graphene-like carbon films on glass at low temperature, J. Phys. D Appl. Phys. 47 (2013), 045305.

[31] H. Bana, E. Travaglia, L. Bignardi, P. Lacovig, C.E. Sanders, M. Dendzik, M. Michiardi, M. Bianchi, D. Lizzit, F. Presel, D. De Angelis, N. Apostol, P. Kumar Das, J. Fujii, I. Vobornik, R. Larciprete, A. Baraldi, P. Hofmann, S. Lizzit, Epitaxial growth of single-orientation high-quality MoS 2 monolayers, 2D Mater. 5 (2018), 035012.

[32] R. Muñoz, L. Martínez, E. López-Elvira, C. Munuera, Y. Huttel, M. García-Hernández, Direct synthesis of graphene on silicon oxide by low temperature plasma enhanced chemical vapor deposition, Nanoscale 10 (26) (2018) 12779–12787.

[33] X. Li, X. Li, X. Zang, M. Zhu, Y. He, K. Wang, D. Xie, H. Zhu, Role of hydrogen in the chemical vapor deposition growth of MoS2 atomic layers, Nanoscale 7 (18) (2015) 8398–8404.

[34] S. Cho, B.S. Kim, B. Kim, W. Kyung, J. Seo, M. Park, J.W. Jeon, K. Tanaka, J. D. Denlinger, C. Kim, D. Odkhuu, B.H. Kim, S.R. Park, Electronic-dimensionality

reduction of bulk MoS2 by hydrogen treatment, PCCP 20 (35) (2018) 23007–23012.

[35] A.C. Ferrari, D.M. Basko, Raman spectroscopy as a versatile tool for studying the properties of graphene, Nat. Nanotechnol. 8 (4) (2013) 235–246.

[36] A.C. Ferrari, J. Robertson, Resonant Raman spectroscopy of disordered, amorphous, C carbon, Phys. Rev. B 64 (2001), 075414.

[37] R. Hawaldar, P. Merino, M.R. Correia, I. Bdikin, J. Grácio, J. Méndez, J.A. Martín-Gago, M.K. Singh, Large-area high-throughput synthesis of monolayer graphene sheet by Hot Filament Thermal Chemical Vapor Deposition, Sci. Rep. 2 (2012), 682–682.

[38] A. Eckmann, A. Felten, A. Mishchenko, L. Britnell, R. Krupke, K.S. Novoselov, C. Casiraghi, Probing the Nature of Defects in Graphene by Raman Spectroscopy, Nano Lett. 12 (8) (2012) 3925–3930.

[39] J. Azpeitia, I. Palacio, J.I. Martínez, I. Muñoz-Ochando, K. Lauwaet, F.J. Mompean, G.J. Ellis, M. García-Hernández, J.A. Martín-Gago, C. Munuera, M.F. López, Oxygen intercalation in PVD graphene grown on copper substrates: A decoupling approach, Appl. Surf. Sci. 529 (2020) 147100.

[40] F. Giannazzo, G. Fisichella, A. Piazza, S. Di Franco, I.P. Oliveri, S. Agnello, F. Roccaforte, Current injection from metal to MoS2 probed at nanoscale by conductive atomic force microscopy, Mater. Sci. Semicond. Process. 42 (2016) 174–178.

[41] F. Giannazzo, E. Schilirò, G. Greco, F. Roccaforte, Conductive Atomic Force Microscopy of Semiconducting Transition Metal Dichalcogenides and Heterostructures, Nanomaterials (Basel) 10 (2020) 803.

[42] F. Giannazzo, I. Deretzis, A. La Magna, F. Roccaforte, R. Yakimova, Electronic transport at monolayer-bilayer junctions in epitaxial graphene on SiC, Phys. Rev. B 86 (2012), 235422.